

Wideband Scattering Diffusion by using Diffraction of Periodic Surfaces and Optimized Unit Cell Geometries

Filippo Costa^{1*}, Agostino Monorchio¹, Giuliano Manara¹

¹ Università di Pisa, Dipartimento di Ingegneria dell'Informazione, Pisa, Via Caruso 16, 56122, Italy.

* Corresponding author: filippo.costa@unipi.it

ABSTRACT

A methodology to obtain wideband scattering diffusion based on periodic artificial surfaces is presented. The proposed surfaces provide scattering towards multiple propagation directions over a wide frequency band. The proposed artificial surfaces comprise unit cells with an optimized geometry and arranged with a repetition period exceeding one wavelength. The large periodicity induces the excitation of multiple Floquet harmonics. The geometry of the elementary unit cell is optimized by imposing the minimization of the fundamental Floquet harmonic reflection coefficient over a wide frequency band. The layout of the FSS is optimized by using a genetic algorithm in conjunction with periodic Method of Moments. The proposed design method is verified through full-wave simulations and measurements. The proposed solution guarantees very good performance in terms of bandwidth thickness ratio and removes the need of a high resolution printing process.

Introduction

The scattering control of objects is today a strategic theme of research. Most of the efforts in the last decade have been dedicated to the design of cloaking devices capable of guiding electromagnetic radiation around objects to make them invisible¹⁻⁴. Cloaking allows also to minimize the scattering of objects but its application is usually restricted to small objects and characterized by particular shapes. The reduction of the electromagnetic signature of objects, in practice, is usually obtained using adequate geometry^{5,6} or through absorbing surfaces which transform electromagnetic radiation into heat⁷⁻⁹. Reduction of electromagnetic signature of objects is a good mean to reduce the detection probability of the most popular device based on retro-reflection, that is, radar. Radar technology is nowadays applied to a wide range of scenarios including many civil applications. Some examples include aircraft radar, air traffic control, speed cameras, automotive high-resolution radar, radio frequency identification (RFID)¹⁰⁻¹³. While in a military scenario the main interest is to reduce Radar Cross Section (RCS) to make a target invisible, in other scenarios, such as RFID or self-driving cars¹³⁻¹⁵, the level of radar cross section may need to be increased to make an obstacles more visible. The increasing of RCS towards specific or energy spreading can be achieved through metamaterials and metasurfaces¹⁶⁻²³. The improved visibility of a target can be obtained through a scattering diffusion technique which consists in spreading of the energy towards multiple direction instead of a single one as it typically happens for planar surfaces.

One of the first approach to achieve scattering diffusion was presented by Paquay et al. in 2007 who employed a combination of Artificial Magnetic Conductors (AMC) and perfect electrical conductor (PEC) cells in a chessboard like configuration¹⁶. The approach has been then extended to wideband operation by using two AMC surfaces maintaining the phase opposition in a certain band¹⁷. Aperiodic designs have been also proposed¹⁸. The energy spreading leads to a reduction of the bistatic contribution. For this reason, scattering diffusion is often interpreted as an alternative to radar absorbing materials for reducing the visibility of a target. The interpretation of the lowered radar cross section towards a specific direction provided in those papers is that the surface leads to a scattering cancellation due to the opposite phases of closely located elements. However, it has to be remarked that chessboard surfaces are designed by using an alternation of macro-cells formed by several elementary unit cells and the periodicity of macro-cells exceeds one wavelength leading to the excitation of grating lobes. The scattering diffusion phenomenon is helped by the proposed lattice since the proposed configuration is not working by using an alternation of simple unit cells. Alternative approaches consist in employing metamaterial coatings with randomly distributed refractive indices¹⁹. The approach of¹⁹ has anyway evident practical implementation problems due to the complexity. More recent papers have also proposed a design procedure which exploits the theoretical background of reflectarray antennas. In this case, the objective is exactly the opposite of the one pursued in the design of a reflectarray antenna, that is, the impinging energy should be deviated as much as possible towards generic directions instead of being focalized. The scattering diffusion effect is therefore obtained with artificial impedance surfaces with non-uniformly distributed reflection phases²⁰⁻²³. The design approach have been proved to provide reasonable wideband operation when used in conjunction with a stochastic optimization approach.

The present paper presents an innovative approach to obtain scattering diffusion. The approach relies on the use of an artificial impedance surface (AIS) comprising a frequency selective surfaces (FSS) placed in the vicinity of an impenetrable surface. The FSS is characterized by a periodicity exceeding one wavelength and this induces the excitation of a high number of Floquet harmonics. The scattering towards high order harmonics is maximized by optimizing the geometry of the unit cell through a genetic algorithm. The objective function used through the optimization process is the minimization of the reflection coefficient of the fundamental harmonic over a wideband. In this way the energy is efficiently spread towards high order harmonics in the whole analyzed frequency band. It is the first time, for the best of our knowledge, that periodic elements with large periodicities are employed to achieve wideband scattering diffusion. The proposed technique does not need subwavelength elements and therefore does not poses strict requirements in terms of precision of lithographic processes. This is an evident advantage for high frequencies and also when large objects with a size of tens of wavelengths have to be covered with these surfaces.

The paper is organized as follows. The section II shows the theoretical background of the scattering from periodic impedance surfaces and the operating principle of the proposed scattering diffusion technique. The third section is dedicated to the description of the optimization process of the FSS geometry. Some representative results are reported in section IV. A visualization of scattered field through scattering patterns on wavevectors planes clarifies also the physical phenomena involved into the wave scattering of the proposed surface. Finally, section V reports measured results on manufactured samples compared to simulated results.

Design approach an theoretical background

When an electromagnetic wave impinges on an interface can be transmitted, reflected or absorbed. The direction of the reflected and transmitted waves follows the Snell law²⁴. However, when the interface is formed by a periodic surface with an inter-element distance exceeding one wavelength, interference phenomena lead scattered waves to be directed towards multiple directions known as diffraction orders or Floquet harmonics^{7,25-27}. The propagation directions are solely determined by the geometry of the lattice on which unit cells of the periodic surface are disposed. In a one dimensional case, the non-specular directions of scattering can be computed according to basic theory of diffraction gratings²⁶. With reference to **Fig. 1a**, due to the spatial periodicity, additional reflected components are characterized by the following in-plane wavevector components:

$$k_{x,scatt} = -k_{x,inc} + \frac{2\pi m}{D} \quad (1)$$

Dividing both members of (1) by the free space wavenumber, k_0 , the scattering angles are derived:

$$\theta_{scatt} = \sin^{-1} \left(\frac{m \cdot \lambda}{D} - \sin(\theta_{inc}) \right) \quad (2)$$

where m represents the harmonic number, D is the inter-element spacing, λ is the operating wavelength, and θ_{inc} is the angle of incidence. Let us suppose having a periodic Frequency Selective Surface (FSS) printed at a certain distance from an impenetrable surface in such way that the transmitted energy is zero. This surface is known as Artificial Impedance Surface (AIS) and its geometry is reported in **Fig. 1a**. The scattered fields are localized towards specific directions, namely the Floquet harmonics. As an example, the direction of Floquet harmonics as a function of frequency, when $\theta_{inc}=30^\circ$, is represented in **Fig. 1b**. Analogously, for a bidimensional periodic array the scattered field goes towards the following directions:

$$\theta_{scatt} = \cos^{-1} \left(\frac{k_z}{k_0} \right); \quad \phi_{scatt} = \tan^{-1} \left(\frac{k_x}{k_y} \right) \quad (3)$$

where k_x , k_y and k_z are the x , y and z components of the wavevector k_0 and are defined as follow²⁸:

$$\begin{aligned} k_x &= k_0 \sin \theta \cos \phi + 2m\pi/D_x; \\ k_y &= k_0 \sin \theta \sin \phi + 2n\pi/D_y; \\ k_z &= \sqrt{k_0^2 - k_x^2 - k_y^2} \end{aligned} \quad (4)$$

where D_x and D_y are the inter-element spacing along x and y directions, (m,n) couples represent the indexes of the Floquet harmonics, θ and ϕ represent the incident angle of the incoming wave. It is evident from the above relations that a certain number of higher order Floquet modes are in propagation when the FSS periodicity exceeds one wavelength. However, the degree of excitation of each Floquet harmonic depends on the specific shape of the FSS unit cell. The total scattered field can be seen as a summation of the harmonic contributions²⁶:

$$E^R = \sum_{i=-\infty}^{+\infty} R_i e^{(jk_i \cdot \vec{r})} \quad (5)$$

Where k_i represent the wavevector of the i^{th} harmonic and r is the propagation direction and R_i represent the reflection coefficient of a specific harmonic, namely towards a specific direction. The energy of a specific harmonic is related to the diffraction

efficiency²⁶. Our objective is to maximize the diffraction efficiency of all exited high order harmonics and thus minimizing the scattered fields toward the bistatic direction. The scattering from impedance surfaces can be seen also with the theory of antenna arrays²⁰ and, in this representation, the geometry of the element determines the element factor whereas the lattice geometry represents the array factor. If the scattering reduction has to be obtained in a narrow frequency band the FSS geometry can be designed by inspecting the surface current distribution but this method is not suitable for designing FSS elements having wideband scattering reduction performance. A good strategy to obtain the desired wideband characteristic of the designed surface, is to obtain the FSS geometry via an optimization algorithm in conjunction with a Method of Moment analysis of the surface.

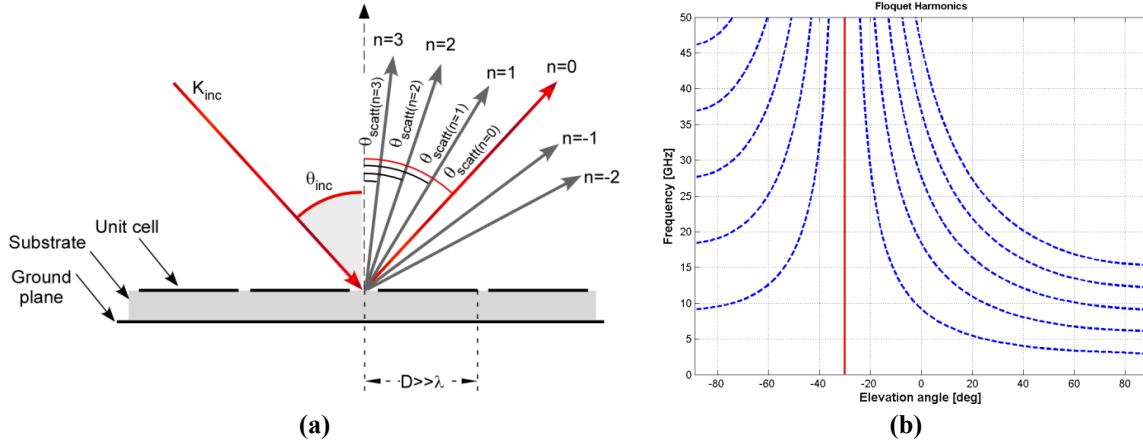


Fig. 1 – (a) Representation of scattering directions for an artificial impedance surface with repetition period exceeding one wavelength. (b) Scattering angle/frequency plot of scattered Floquet harmonics for an incident angle of $\theta=30^\circ$ and $\varphi=0^\circ$.

Optimization process

As already pointed in the previous section, the objective of this work is to design low-profile impedance surfaces able to spread the impinging energy via scattering diffusion and at the same time, drastically reduce bistatic reflection over a wide frequency band. To achieve this behaviour, a thin artificial impedance surface (AIS), whose geometry is reported in Fig. 1, is opportunely designed. The AIS surface is formed by a metallic backed substrate with a frequency selective surface printed on top. In order to excite a high number of Floquet harmonics and thus allow multiple propagation directions, the periodicity of the FSS is chosen to be larger than one wavelength. In addition, the geometry of the FSS element is optimized to guarantee an efficient transferring of energy from fundamental Floquet harmonic to high order ones (high diffraction efficiency). The optimization is performed through a genetic algorithm (GA). To this purpose, the FSS unit cell is discretized with a regular mesh composed by 16×16 pixels. The pixel can be made of metal or not and this binary information is stored in a 16 by 16 matrix²⁹. In order to concentrate the optimization process on the FSS geometry only, the dielectric substrate is a priori decided. The optimizer is supported by a Periodic Method of Moments (PMM) code based on roof-top basis functions³⁰. At the end of the optimization process, the unit cell geometry is double-checked to avoid isolated pixels where any basis function are not defined. The objective function consists in minimizing the reflection coefficient of the fundamental Floquet harmonic over a number of frequency points over a wideband. Being the unit cell periodicity larger of the operating wavelength, issues about the accuracy of the mesh may rise. Indeed, the discretization of $1/16$ with respect to the unit cell periodicity may not be sufficient if the periodicity is too large with respect to the operating wavelength. For this reason, the maximum allowed periodicity of 4λ at the maximum operation frequency is imposed and the accuracy of the optimal solution found by the GA algorithm is verified, at the end of the optimization process, with a 32×32 mesh. A direct optimization with a mesh of 32×32 is not possible because of the prohibitive computation burden.

Numerical Results

Two representative examples are shown to demonstrate the validity of the proposed approach. Both low and high permittivity substrates are employed to assess the effect of the substrate permittivity. In the first example, name configuration A for convenience, the substrate is set to be a foam spacer ($\epsilon_r=1.05$) with a thickness of 3 mm whereas, in the configuration B, the substrate is standard 2 mm thick FR4 characterized by a higher dielectric permittivity value ($\epsilon_r=4.4$). The unit cell geometries and the periodicity values are optimized through a genetic algorithm. The optimized unit cell geometries are reported in Fig. 2. The periodicities are set to 40.5 mm and 29.2 mm for the configuration A and B respectively. The use of low-permittivity substrates provides better results in terms of bistatic reflectivity reduction with respect to high-permittivity substrates. For sake of brevity, the performance of the configuration B will be reported in the measurement section. The optimized reflection coefficient

amplitude of the fundamental harmonic ($m=0, n=0$) for the configuration A at normal incidence is reported in Fig. 3. The results obtained with the rough mesh used during the optimization process compares quite well with the more accurate solution obtained by using a considerable higher number of basis functions (discretization pixel equal to $D/32$).

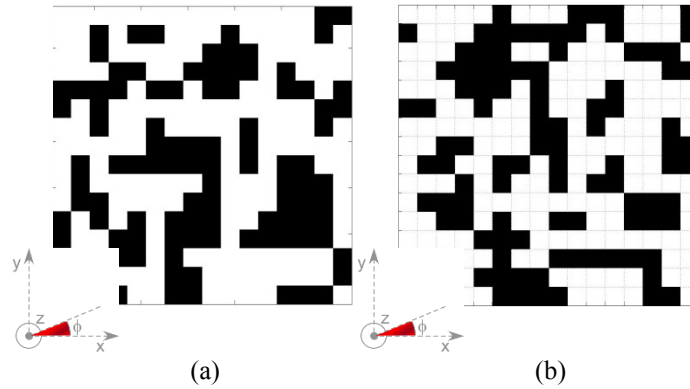


Fig. 2 – Two unit cell geometries obtained by optimizer. (a) Configuration A with air substrate of 3 mm. (b) Configuration B with FR4 substrate of 2.4 mm.

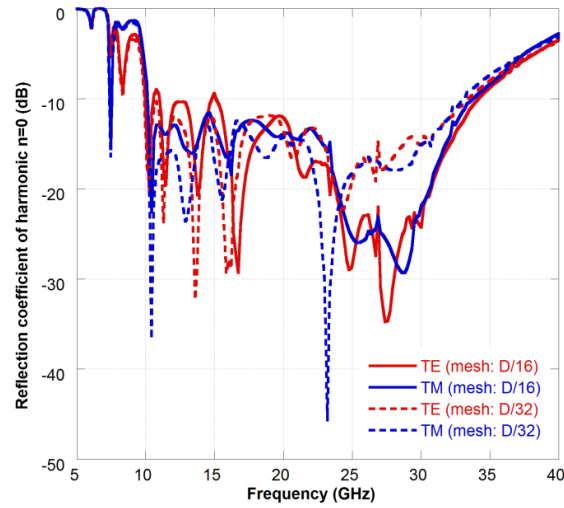


Fig. 3 – Reflection coefficient of the fundamental harmonic ($m=0, n=0$) for the configuration A computed with a rough mesh ($D/16$) and with a more accurate one ($D/32$).

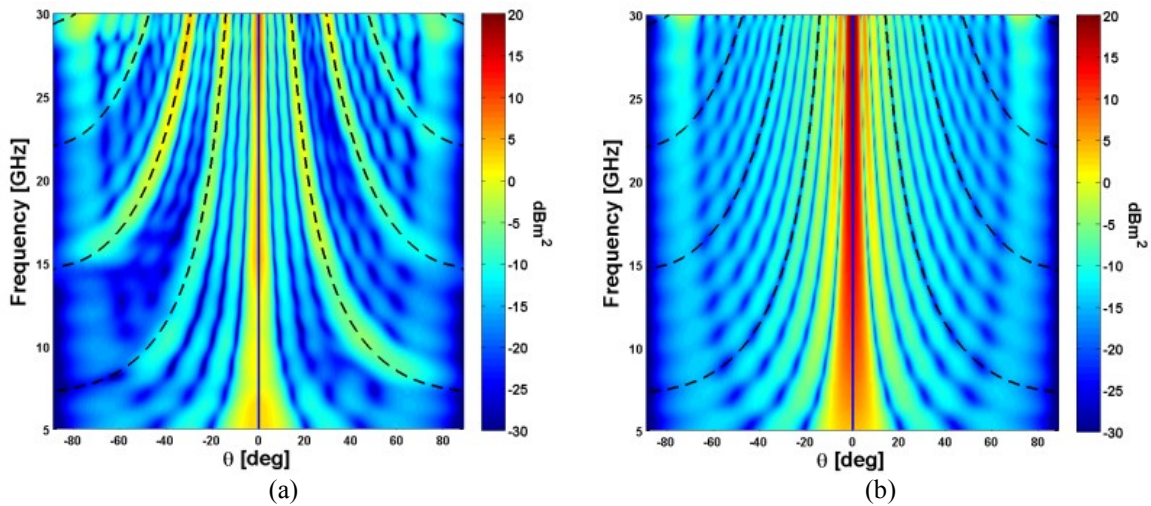


Fig. 4 – Radar cross section as a function of frequency and elevation incidence angle. The RCS is plotted on the plane $\phi=0^\circ$. (a) Designed surface (configuration A) and PEC plane of the same dimension. The size of the surface is 162 mm^2 and the impinging plane wave come from $\theta=0^\circ, \phi=0^\circ$. Dashed lines represents the directions of high order Floquet harmonics obtained by using relation (2).

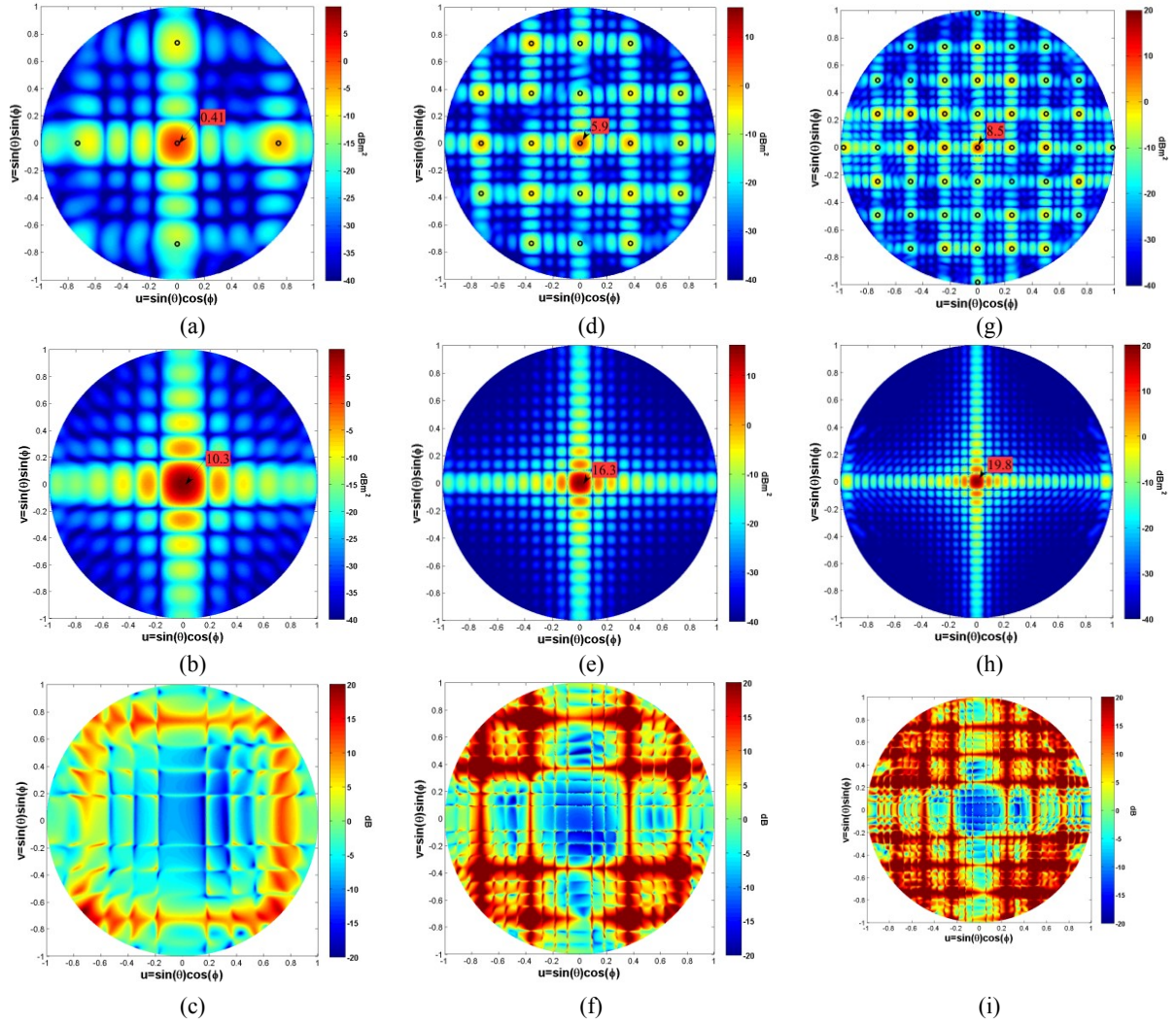


Fig. 5 – Scattering patterns on wave vector domain for the proposed artificial impedance surface, for a PEC surface of the same dimension (162 mm^2) and difference between the two at three representative frequencies: (a) Metasurface 10 GHz, (b) PEC 10 GHz, Difference 10 GHz, (d) Metasurface 20 GHz, (e) PEC 20 GHz, difference 20 GHz, (g) Metasurface 30 GHz, (h) PEC 30 GHz, (i) difference 30 GHz. The impinging plane wave comes from $\theta=0^\circ$, $\phi=0^\circ$.

A deeper analysis of the configuration A in terms of RCS diagrams is necessary in order to understand the physical behavior of the designed device. To this purpose a finite version of the designed impedance surface is analyzed by using Ansoft HFSS. The analyzed surface comprises a repetition of four by four unit cells. The geometry of the unit cell is shown in Fig. 2a and the repetition period is 40.5 mm. The total dimension of the surface is 162 mm^2 . In Fig. 4, the radar cross section of the artificial impedance surface is reported on a principal phi cut ($\phi=0^\circ$) and as a function of elevation angle θ on the abscissa and of the frequency on the ordinate. The propagation direction of the Floquet harmonics, computed according to relation (2), are superimposed by using black dashed lines. As it is evident, the designed surface provides an efficient spreading of the impinging energy towards the predicted high order harmonics contrarily to the metallic surface (Fig. 4b). The number of harmonics increases proportionally to the operating frequency. Even if very useful, the phi-cut representation of the scattered fields does not predict all the possible propagation directions or, in other words, all the Floquet harmonics. Indeed, some of the energy is redirected towards directions outside of the principal planes. The additional harmonics can be easily predicted by using the relations (3) and (4) valid for the 2D case.

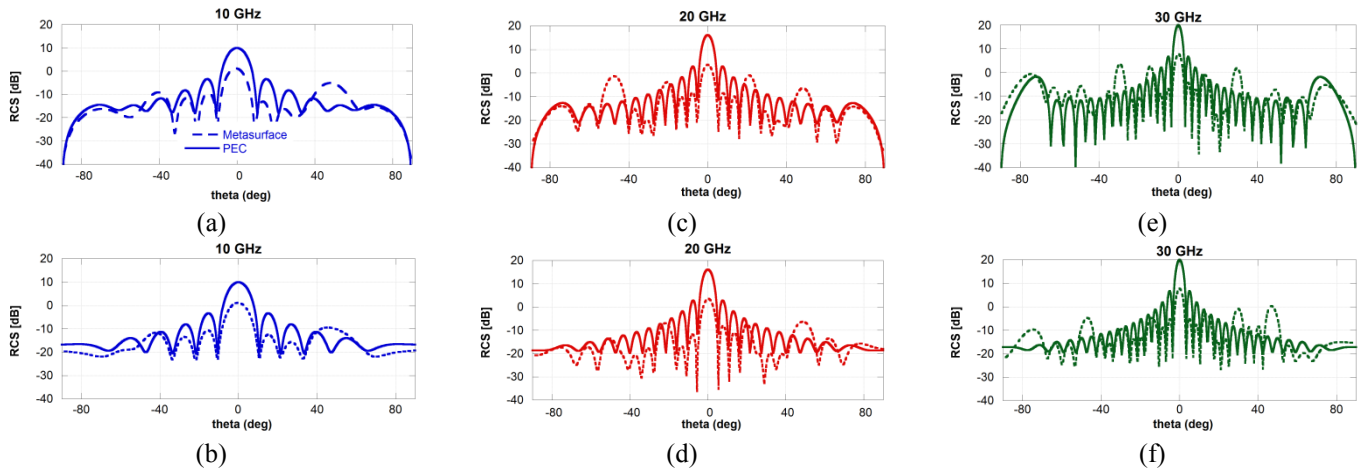


Fig. 6 – Scattering pattern of impedance surface and for a PEC surface on the two main planes at three representative frequencies: (a) 10 GHz, $\varphi=0^\circ$, (b) 10 GHz, $\varphi=90^\circ$, (c) 20 GHz, $\varphi=0^\circ$, (d) 20 GHz, $\varphi=90^\circ$, (e) 30 GHz, $\varphi=0^\circ$, (f) 30 GHz, $\varphi=90^\circ$.

To provide a clear visualization of the scattered energy over the phi and theta cuts, the scattering patterns on the normalized wavevector domain ($u=\sin(\theta)\cos(\varphi)$ and $v=\sin(\theta)\sin(\varphi)$) are plotted in Fig. 5 for three representative frequencies ($f=10$ GHz, $f=20$ GHz, $f=30$ GHz). The radar cross section of the designed surface is reported on the left whereas the radar cross section of a PEC surface with the same dimension is reported on the right for comparison. The incident angle of the impinging plane wave is set to $\theta=0^\circ$, $\varphi=0^\circ$. The propagation directions predicted by the relations (3) and (4), superimposed on the colour plots by using black circles, agree very well with the one obtained with the numerical full-wave analysis. By simply subtracting the RCS of the impedance surface and the PEC surface, one can obtain the amount of reflectivity reduction/increasing. Indeed, as it is shown in Fig. 5 for the frequencies 10 GHz, 20 GHz and 30 GHz, the designed artificial impedance surface provides a reflectivity reduction of the central zone (bistatic reflection for normal incidence) and an increase of the scattered energy towards other angles.

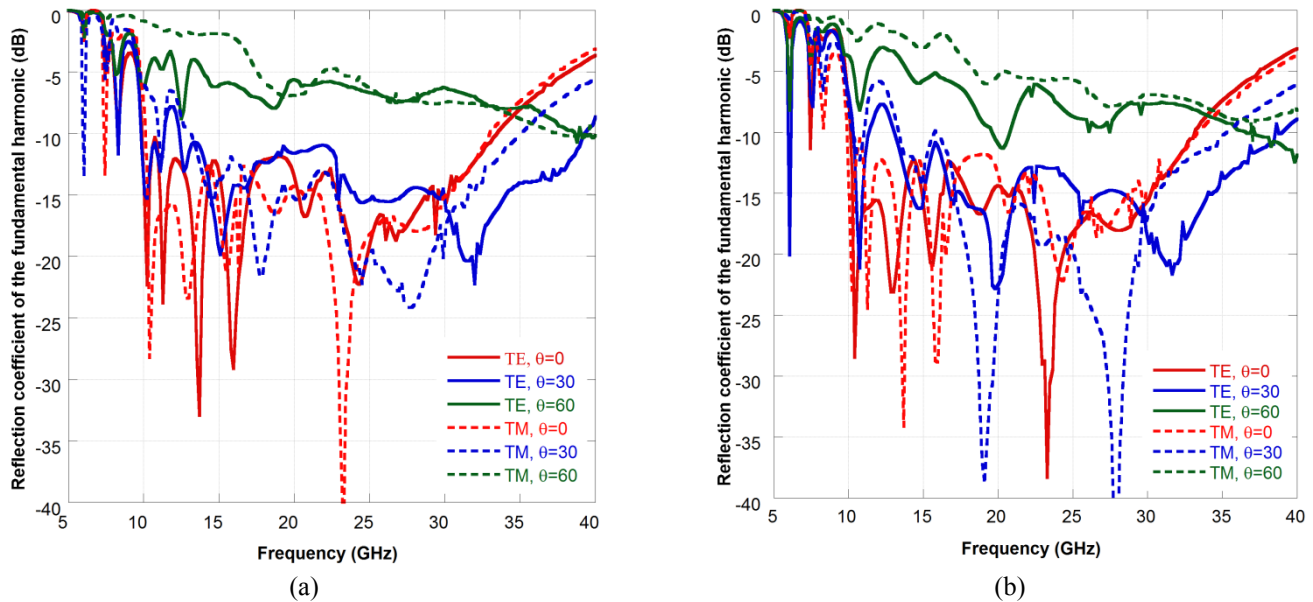


Fig. 7 – Reflection coefficient of the fundamental harmonic ($m=0$, $n=0$) for oblique incident angles. Impinging wave on cut (a) $\varphi=0^\circ$ and (b) $\varphi=90^\circ$.

The scattered energy patterns tends to become more uniform as the frequency rises because of the high number of excited harmonics. For an easier assessment of the difference between the scattered field of the proposed surface and the PEC plane, the conventional 2D Cartesian scattering patterns are shown in Even if designed for normal incidence, the surface maintains bistatic RCS reduction properties also for oblique incidence. Indeed, as shown in the diagram of Fig. 1, the unique contribution towards bistatic direction is due to the fundamental Floquet harmonic. In Fig. 7, the reflection coefficient of the fundamental harmonic ($n=0$, $m=0$) is shown for $\theta=0^\circ$, 30° and 60° . The performance are reported in Fig. 6 both for a wave impinging on the phi-cut $\varphi=0^\circ$ and on the phi-cut $\varphi=90^\circ$. The reflectivity reduction is stable up to 30° and then it degrades for $\theta=60^\circ$. As previously

shown, we can represent the scattering of the surface on the (u, v) domain to get a clearer visualization of the scattered fields. The plots are shown in Fig. 8 for two representative frequencies (20 GHz and 30 GHz) and for an impinging wave coming from $\theta=-45^\circ$, $\varphi=90^\circ$. While the PEC plane redirects all the impinging energy towards the bistatic scattering angle predicted by the Snell law, the impedance surface tends to spread the energy also on additional directions determined by the propagating harmonics. The efficiency in spreading the energy towards the high-order harmonics depends on the shape of the unit cell. As before, the propagation directions predicted by using (3) and (4) are superimposed on the scattering pattern of the impedance surface by using black circles. The energy is indeed concentrated around the allowed propagation directions.

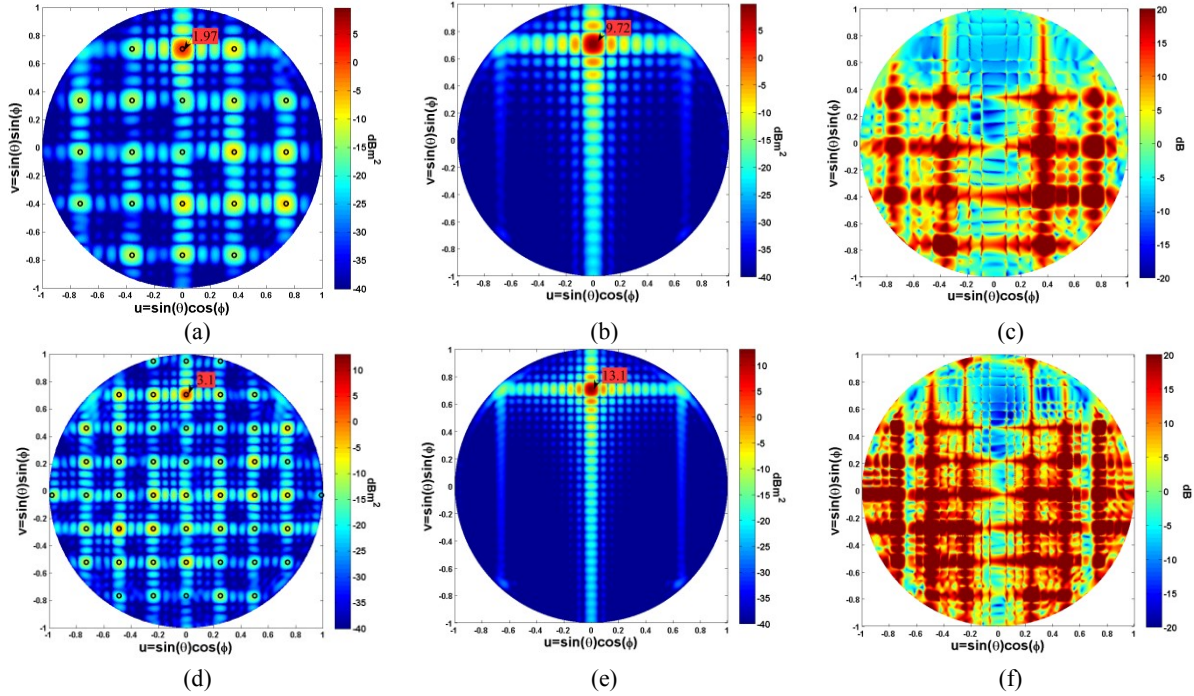


Fig. 8 – Scattering patterns on wave vector domain for oblique incidence. The impinging plane wave come from $\theta=-45^\circ$, $\varphi=90^\circ$. (a) Metasurface 20 GHz, (b) PEC 20 GHz, Difference 20 GHz, (d) Metasurface 30 GHz, (e) PEC 30 GHz, difference 30 GHz.

Measured results

To verify the reliability of MoM periodic simulations and FEM based simulations presented in previous sections, some prototypes have been manufactured and measured. The configuration A, whose performance have been extensively discussed in the previous section, is manufactured by printing the FSS pattern on a thin Kapton substrate. The thin layer has been then glued to a 3 mm thick Rohacell substrate backed by an aluminum foil. The second prototype is made with a 2 mm thick FR4 and it has been fabricated to investigate the effect of using high-permittivity substrates. The photographs of the manufactured samples are shown in Fig. 9. The unit cell geometries are the ones shown in Fig. 2.

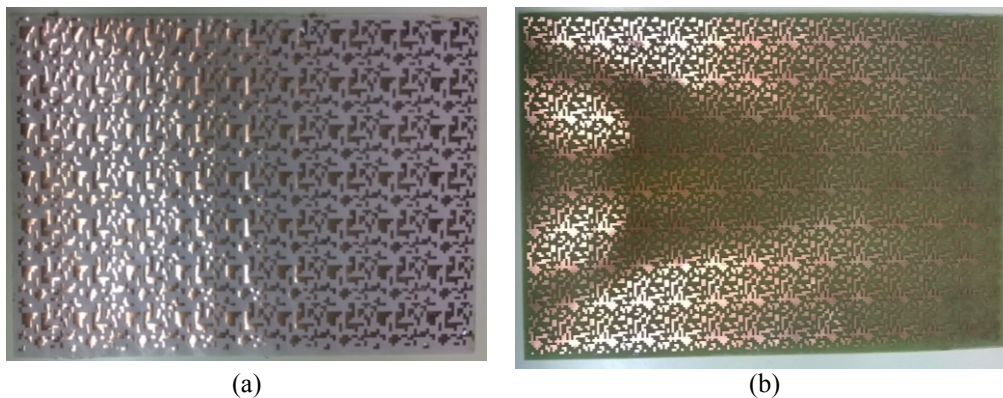


Fig. 9 – Pictures of the prototypes. (a) Configuration A, (b) configuration B.

In Fig. 10 the measured reflectivity reduction of the impedance surfaces at normal incidence are shown. The results are compared both with the results of the MoM approach used for the optimization process and with the numerical results obtained by simulating the a finite surface comprising 4x4 unit cells with HFSS. The results are in a reasonable agreement even if there are differences due to the infinite extent approximation and to the coarse mesh discretization used in the MoM approach. The use of a substrate with a higher permittivity allows reducing the thickness of the surface but it provides worse performance in terms of RCS reduction of the bistatic reflected fields.

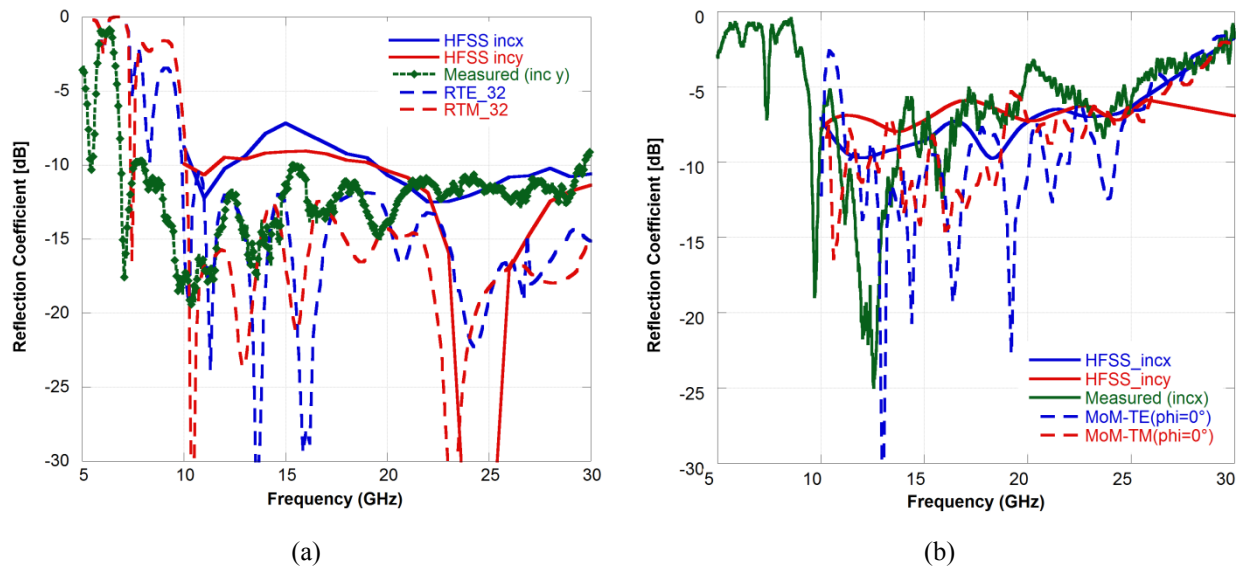


Fig. 10 – (a) Measured reflection coefficient at normal incidence for the finite impedance surfaces: (a) unit cell reported in Fig. 2a. The periodic surface is printed on a thin kapton substrate and then glued to a grounded 3 mm Rohacell dielectric slab. The size of the manufactured sample is 285 mm by 366 mm. (b) unit cell reported in Fig. 2b. The periodic surface is printed on a 2 mm thick FR4 substrate backed by a ground plane. The size of the manufactured sample is 290 mm by 380 mm.

Conclusion

An innovative method for obtaining bistatic scattering reduction by using the diffusion of scattered fields towards generic directions is proposed. The approach exploits impedance surfaces formed by frequency selective surfaces with a periodicity exciding one wavelength. The geometry of the FSS cells is optimized in order to maximize the energy directed on high order Floquet harmonics over a very-large frequency band. A scattering diffusion, with a 10 dB reduction of the fundamental harmonic reflection, is obtained from 7 GHz to 30 GHz with a 3 mm thick surface. The scattering phenomenon is explained via Floquet theory and by using insightful colon scattering patterns on wavevectors domain. The results are confirmed by simulations and measurements on finite size samples.

Methods

The response of the low-bistatic scattering surfaces have been measured through a couple of horn antennas operating between 2 GHz and 20 GHz. Two Teledyne Reynolds cables have been employed for connecting the antennas to the VNA. The cables introduce acceptable losses up to 26 GHz. The employed VNA is the PNA-L N5230C which works up to 50 GHz. The measurements have been performed at normal incidence by using a bistatic configuration of the antennas. Even if the measured results can be considered accurate up to 20 GHz because of the equipment limitations, they are plotted up to 30 GHz.

References

1. Alitalo, P. & Tretyakov, S. Electromagnetic cloaking with metamaterials. *Materials Today* **12**, 22–29 (2009).
2. Alù, A. & Engheta, N. Achieving transparency with plasmonic and metamaterial coatings. *Phys. Rev. E* **72**, 016623 (2005).
3. Soric, J. C. *et al.* Controlling Scattering and Absorption With Metamaterial Covers. *IEEE Transactions on Antennas and Propagation* **62**, 4220–4229 (2014).

4. Selvanayagam, M. & Eleftheriades, G. V. Experimental Demonstration of Active Electromagnetic Cloaking. *Phys. Rev. X* **3**, 041011 (2013).
5. Knott, E. F., Shaeffer, J. & Tuley, M. *Radar Cross Section, Second Edition*. (SciTech Publishing, 2004).
6. Ufimtsev, P. Y. Comments on diffraction principles and limitations of RCS reduction techniques. *Proceedings of the IEEE* **84**, 1830–1851 (1996).
7. Munk, B. A. *Frequency Selective Surfaces: Theory and Design*. (John Wiley & Sons, 2005).
8. Costa, F., Monorchio, A. & Manara, G. Analysis and design of ultra thin electromagnetic absorbers comprising resistively loaded high impedance surfaces. *IEEE Transactions on Antennas and Propagation* **58**, 1551–1558 (2010).
9. Tao, H. *et al.* A metamaterial absorber for the terahertz regime: design, fabrication and characterization. *Optics Express* **16**, 7181 (2008).
10. Wenger, J. Automotive radar - status and perspectives. in *IEEE Compound Semiconductor Integrated Circuit Symposium, 2005. CSIC '05* 4 pp.– (2005). doi:10.1109/CSICS.2005.1531741
11. Nolan, M. *Fundamentals of Air Traffic Control*. (Cengage Learning, 2010).
12. Skolnik, M. I. *Radar applications*. (1988).
13. Finkenzeller, K. & Waddington, R. *RFID handbook: radio-frequency identification fundamentals and applications*. (Wiley New York, 1999).
14. Guizzo, E. How Google's Self-Driving Car Works. (2011). at <<http://spectrum.ieee.org/automaton/robotics/artificial-intelligence/how-google-self-driving-car-works>>
15. Bertozzi, M., Broggi, A. & Fascioli, A. Vision-based intelligent vehicles: State of the art and perspectives. *Robotics and Autonomous Systems* **32**, 1–16 (2000).
16. Paquay, M., Iriarte, J.-C., Ederra, I., Gonzalo, R. & de Maagt, P. Thin AMC Structure for Radar Cross-Section Reduction. *IEEE Transactions on Antennas and Propagation* **55**, 3630–3638 (2007).
17. Zhang, Y., Mittra, R., Wang, B.-Z. & Huang, N.-T. AMCs for ultra-thin and broadband RAM design. *Electronics Letters* **45**, 484 (2009).
18. Edalati, A. & Sarabandi, K. Wideband, Wide Angle, Polarization Independent RCS Reduction Using Nonabsorptive Miniaturized-Element Frequency Selective Surfaces. *IEEE Transactions on Antennas and Propagation* **62**, 747–754 (2014).
19. Yang, X. M., Zhou, X. Y., Cheng, Q., Ma, H. F. & Cui, T. J. Diffuse reflections by randomly gradient index metamaterials. *Opt. Lett.* **35**, 808–810 (2010).
20. Wang, K., Zhao, J., Cheng, Q., Dong, D. S. & Cui, T. J. Broadband and Broad-Angle Low-Scattering Metasurface Based on Hybrid Optimization Algorithm. *Sci. Rep.* **4**, (2014).

21. Yang, X. M., Jiang, G. L., Liu, X. G. & Weng, C. X. Suppression of Specular Reflections by Metasurface with Engineered Nonuniform Distribution of Reflection Phase. *International Journal of Antennas and Propagation* **2015**, e560403 (2015).
22. Gao, L.-H. *et al.* Broadband diffusion of terahertz waves by multi-bit coding metasurfaces. *Light Sci Appl* **4**, e324 (2015).
23. Song, Y., Ding, J., Guo, C., Ren, Y. & Zhang, J. Ultra Broadband Backscatter Radar Cross Section Reduction Based on Polarization In-sensitive Metasurface. *IEEE Antennas and Wireless Propagation Letters* **PP**, 1–1 (2015).
24. Blackstock, D. T. *Fundamentals of Physical Acoustics*. (John Wiley & Sons, 2000).
25. Palmer, C. A., Loewen, E. G. & Thermo, R. G. L. *Diffraction grating handbook*. (Newport Corporation Springfield, OH, 2005).
26. Gaylord, T. K. & Moharam, M. G. Planar dielectric grating diffraction theories. *Appl. Phys. B* **28**, 1–14 (1982).
27. Cope, T. D. The rittenhouse diffraction grating. *Journal of the Franklin Institute* **214**, 99–104 (1932).
28. Garcia-Vigueras, M., Mesa, F., Medina, F., Rodriguez-Berral, R. & Gomez-Tornero, J. L. Simplified Circuit Model for Arrays of Metallic Dipoles Sandwiched Between Dielectric Slabs Under Arbitrary Incidence. *IEEE Transactions on Antennas and Propagation* **60**, 4637–4649 (2012).
29. Manara, G., Monorchio, A. & Mittra, R. Frequency selective surface design based on genetic algorithm. *Electronics Letters* **35**, 1400–1401 (1999).
30. Mittra, R., Chan, C. H. & Cwik, T. Techniques for analyzing frequency selective surfaces-a review. *Proceedings of the IEEE* **76**, 1593–1615 (1988).

Author contributions statement

F.C. conceived the idea, conducted simulations and measurements and prepared the manuscript. A.M. and G.M. analysed the results, suggested modifications and reviewed the manuscript.

Competing financial interests

The authors declare no competing financial interests.